HTML ABSTRACT + LINKS

JOURNAL OF APPLIED PHYSICS **97**, 114304 (2005)

Physical models for coupled electromechanical analysis of silicon nanoelectromechanical systems

Zhi Tang, Yang Xu, Gang Li, and N. R. Aluru[a)]

Department of Mechanical and Industrial Engineering, Beckman Institute for Advanced Science and Technology, University of Illinois at Urbana–Champaign, Urbana, Illinois 61801

(Received 28 July 2004; accepted 4 March 2005; published online 24 May 2005)

Nanoelectromechanical systems (NEMS) can be designed and characterized by understanding the interaction and coupling between the mechanical, electrical, and the van der Waals energy domains. In this paper, we present physical models and their numerical simulation for coupled electrical and mechanical analysis of silicon NEMS. A nonlinear continuum elastic model is employed for mechanical analysis. The material properties required in the continuum model are extracted from molecular-dynamics simulations. We present three electrostatic models—namely, the classical conductor model, the semiclassical model, and the quantum-mechanical model, for electrostatic analysis of NEMS at various length scales. The electrostatic models also account for the corrections to the energy gap and the effective mass due to the strain in the silicon nanostructure. A continuum layer approach is introduced to compute the van der Waals forces. The coupling between the mechanical, electrical, and the van der Waals energy domains as well as their numerical implementation is described. Numerical results are presented for several silicon NEM switches to understand the static electromechanical pull-in behavior. © *2005 American Institute of Physics*.
[DOI: 10.1063/1.1897483]

I. INTRODUCTION

Microelectromechanical systems (MEMS) have found widespread applications in many areas including communications, information technology, medical, mechanical, and aerospace technologies.[1] Nanoelectromechanical systems (NEMS) are MEMS with submicron critical dimensions. NEMS have the potential to offer even better solutions to many of the above-mentioned application areas as they can attain fundamental frequencies in the microwave range, mechanical quality factors in the tens of thousands, force sensitivities at the attonewton level, active masses in the femtogram range, mass sensitivity at the level of individual molecules, heat capacities far below a yoctocalorie, etc.[2,3] Although NEMS can be designed using a variety of materials including silicon, silicon carbide, single and multiwall carbon nanotubes, and other materials, silicon is one of the most actively investigated materials for many nanotechnology applications because of its technological importance. Recent papers have demonstrated the use of silicon as nanotweezers[4] and nanoresonators.[5] Silicon nanoswitches are a class of NEM devices with potential applications in mass memory storage, high-frequency electrical switches, and mass or force sensors.

The design and characterization of NEMS can be accelerated by developing accurate physical theories and computational design tools that describe the motion and operation of NEMS. Microelectromechanical systems have been analyzed using the classical physical models or continuum theories[6–8] for the mechanical (elastostatic or elastodynamic) and the electrical (electrostatic) energy domains. However, the physical models and the computational design tools that have been developed for MEMS may not be directly applicable for NEMS because of the small scales encountered in NEMS. For example, van der Waals forces, which can be neglected for MEM devices, can become important for NEMS. In addition, the mechanical and the electrical behavior as well as the coupling between the mechanical and the electrical energy domains could be different for nanoscale structures, necessitating a proper understanding and the development of accurate physical theories for NEMS.

Molecular-dynamics (MD) simulations can be used for nanoscale structural or mechanical analysis. However, because of the large number of atoms involved (typically over one million atoms are required for practical NEM devices) and the small time steps (typically 1 fs) required, MD simulation of a system, even for a nanosecond time scale, is very expensive and practically impossible for device design or optimization. An alternative is to use the classical continuum elasticity theory,[6] but with proper improvements or enhancements. Previous molecular-dynamics simulations for ideal structures appear to indicate that the atomistic behavior becomes manifested only at the truly molecular scale, i.e., of the order of tens of lattice constants in cross section.[9] Hence, for ideal structures (e.g., no defects) with cross-sectional areas larger than a few nm^2, it appears that the continuum approximation could be adequate. In this paper, we employ a geometrically nonlinear continuum elastostatic model with MD-corrected material properties for structural or mechanical analysis of NEMS.

Electrostatic analysis of MEMS assumes that the microstructures can be treated as conductors. In this case all the charges distribute on the surface of the conductors and the coupling between the electrical and the mechanical domains

[a)]Author to whom correspondence should be addressed; electronic mail: aluru@uiuc.edu; URL:http://www.uiuc.edu/~aluru

 © 2005 American Institute of Physics

Downloaded 25 May 2005 to 130.126.121.152. Redistribution subject to AIP license or copyright, see http://jap.aip.org/jap/copyright.jsp

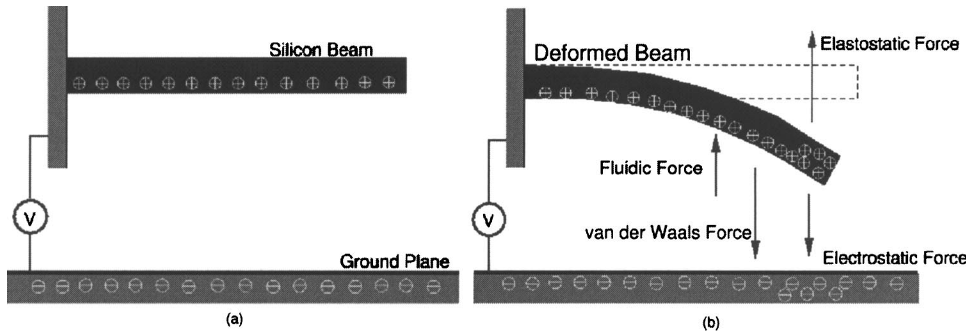

FIG. 1. (a) A silicon beam over a ground plane. Charges are induced on the beam and the ground plane when a potential ($V \neq 0$) is applied. (b) Deformed position of the beam when $V \neq 0$. Note that the charges redistribute as the beam deforms.

is through the electrostatic force which acts only on the surface of the conductors. The conductor assumption may not hold for some NEM devices as silicon nanostructures are more appropriately treated as semiconductors and the charges distribute not only on the surface but also in the bulk of the semiconductor. When the charges are distributed in the bulk, the electrical and the mechanical domains are coupled not only through the surface but also through the bulk or the volume of the semiconductors. In addition, for nanoscale structures the energy gap and the effective mass of the semiconductor can change with the strain in the semiconductor leading to more complicated interaction or coupling between the mechanical and the electrical energy domains. In this paper, we consider three electrostatic models—namely, the classical model, the semiclassical model, and the quantum-mechanical model. We discuss the length scales at which these models can be used and also describe the coupling of the three electrostatic models with the physical model for the mechanical energy domain.

van der Waals interactions can play an important role for the small gaps encountered in NEMS. The direct method to calculate the van der Waals forces is to sum over all the pair atoms in the NEM device. The computational complexity of the direct method scales as $O(n^2)$, where n is the number of atoms in the system. For large systems, the calculation of the van der Waals forces by the direct summation method can be inefficient. In this paper, we develop a continuum layer approach to compute the van der Waals forces. This approach significantly reduces the computational cost. The accuracy of the approach is assessed by comparing the results with the direct summation method. The coupling of the van der Waals energy domain with the electrical and the mechanical energy domains is also discussed.

The rest of the paper is organized as follows. In Sec. II, we introduce the operation of a simple NEM device, a nanoswitch, that will be used to test the various physical or continuum models discussed in this paper. The physical models employed for the mechanical, electrical, and the van der Waals energy domains are discussed in Secs. III–V respectively. The corrections to the energy gap and the effective mass due to the strain in the silicon device are discussed in Sec. VI. The integration of all models is summarized in Sec. VII. The electromechanical behavior of several nanoswitches is investigated in Sec. VIII. Finally, conclusions are presented in Sec. IX.

II. NEM SWITCHES: DEVICE PHYSICS

NEMS typically contain one or more mechanical components which undergo deformation when subjected to electrostatic actuation. Figure 1 shows a typical nanoswitch. The nanoswitch consists of a beam structure that is clamped at one end and the beam is separated from the ground electrode by a small gap. When a voltage is applied between the beam structure and the ground electrode, a charge distribution is induced in the beam and on the ground electrode. The charge distribution gives rise to an electrostatic force which causes the beam to deform. When the beam changes shape, the charge redistributes in the structure(s) and the electrostatic force also changes. In addition to the electrostatic force, when the gap between the beam structure and the fixed electrode is sufficiently small, van der Waals interactions between the structures can become significant. Furthermore, the van der Waals force changes as the beam structure deforms and the gap changes. In addition, if there is a fluid surrounding the beam structure and the fixed electrode, the fluid forces acting on the surface of the structure(s) can change the deformation of the beam. As shown in Fig. 1, an equilibrium state of the electromechanical system is obtained when the mechanical forces (elastic forces) balance with the electrostatic, van der Waals, and the fluidic forces. We assume that the nanoscale electromechanical systems operate in vacuum and neglect the fluidic forces in this paper.

We consider two types of NEM switches, namely, (a) a double-clamped (fixed–fixed) switch and (b) a side-clamped (cantilever) switch. In both cases, the top and the bottom surfaces of the switches and the substrate are taken to be parallel to a (001) plane. The electromechanical analysis of NEM switches involves the modeling of three coupled energy domains: elastostatic, electrostatic, and the van der Waals energy domains. The modeling of these energy domains is discussed in the following sections. We focus on two-dimensional (2D) problems in this paper but the modeling approaches can be extended for three-dimensional problems.

III. ELASTOSTATIC MODELS

The continuum mechanics theory is widely used for mechanical analysis of microstructures.[6,7] The governing equations for the continuum elastostatic analysis on an arbitrary domain Ω are given by[10]

$$\nabla \bullet (\mathbf{FS}) + \mathbf{B} = 0 \quad \text{in } \Omega, \tag{1}$$

Downloaded 25 May 2005 to 130.126.121.152. Redistribution subject to AIP license or copyright, see http://jap.aip.org/jap/copyright.jsp

$$\mathbf{u} = \mathbf{G} \quad \text{on } \Gamma_g, \tag{2}$$

$$\mathbf{PN} = \mathbf{T} \quad \text{on } \Gamma_h, \tag{3}$$

where $\mathbf{F}$ is the deformation gradient given by

$$\mathbf{F} = \mathbf{I} + \nabla \mathbf{u}, \tag{4}$$

$\mathbf{u}$ is the displacement vector from the initial configuration $\mathbf{X}$ to the deformed configuration $\mathbf{x}$, $\mathbf{x}=\mathbf{X}+\mathbf{u}$, $\mathbf{I}$ is the identity tensor, $\mathbf{N}$ is the unit outward normal vector in the initial configuration, $\mathbf{B}$ is the body force vector per unit undeformed volume, $\mathbf{G}$ is the prescribed displacement vector on the boundary portion Γ_g, $\mathbf{T}$ is the surface traction vector per unit undeformed area on the boundary Γ_h, and $\mathbf{P}$ is the first Piola–Kirchhoff stress tensor given by

$$\mathbf{P} = \mathbf{FS}, \tag{5}$$

where $\mathbf{S}$ is the second Piola–Kirchhoff stress given by

$$\mathbf{S} = \mathbf{CE}, \tag{6}$$

$\mathbf{E}$ is the Green–Lagrange strain,

$$\mathbf{E} = \frac{1}{2}(\mathbf{F}^T\mathbf{F} - \mathbf{I}), \tag{7}$$

and $\mathbf{C}$ is the material tensor. Specifically, for the 2D plane strain situation, which is considered in this paper, the material tensor reduces to a 3×3 matrix of the form

$$\mathbf{C} = \frac{Y}{(1+\upsilon)(1-2\upsilon)} \begin{pmatrix} 1-\upsilon & \upsilon & 0 \\ \upsilon & 1-\upsilon & 0 \\ 0 & 0 & 1-2\upsilon \end{pmatrix}, \tag{8}$$

where Y is Young's modulus and υ is Poisson's ratio.

For nanoscale structures, the use of continuum mechanics theory [Eqs. (1)–(8)] can be questionable if there are defects or inhomogeneities present in the structure. Extended continuum mechanics theories or multiscale methods[11] are currently being developed to address this issue. In this paper, we will consider ideal silicon structures that can be treated by the continuum mechanics theory. However, the use of the bulk material properties—that are typically accurate for microscale and bigger structures—can be questionable. This is because, at nanoscale, the generally defined elastic constants depend not only on the material but also on the device geometry. For example, even though surface reconstruction can be neglected for MEM structures, it can affect the elastic properties of NEM structures. MD simulations can be used to capture the atomic-scale characteristics of nanoscale structures. However, MD simulations are expensive and can be impractical for analysis of large and real systems. The approach taken in this paper is to retrieve the elastic constants from molecular-dynamics, and to use these constants in the continuum mechanics theory. By combining the advantages of the continuum theory and the molecular-dynamics, this approach provides an efficient and accurate way for nanoscale structural analysis.

Calculating the elastic constants efficiently and accurately is important since these constants are directly employed in the continuum theory. There are several ways of calculating the elastic constants. In Ref. 12, Ray and Rahman calculated the adiabatic elastic constants using a fluctuation formula appropriate for the microcanonical (*EhN*) ensemble using molecular-dynamics. Karimi *et al.*[13] calculated the elastic constants of a bulk silicon crystal with an isoenthalpic–isotension–isobaric (*HtN*) ensemble using a Monte Carlo technique. In Ref. 14, the fluctuation formulas for obtaining the elastic constants of an arbitrary system are summarized. Although these analytical methods are accurate and converge rather quickly, we will not use them because handling the crystal surface effect at nanoscale using an analytical method can be nontrivial for potentials that have terms beyond pair interactions (e.g., Tersoff potential). Instead, we adopt the direct or the traditional method to retrieve the elastic constants from molecular-dynamics simulations. The traditional method is based on the fact that Young's modulus is defined as the stress divided by the strain for a tensile stress acting in one direction, with the sides of the specimen left free, and Poisson's ratio is defined as the ratio of the transverse contraction strain to the longitudinal extension strain in the direction of the stretching force. We carry out a uniaxial tension test by using molecular-dynamics and retrieve Young's modulus and Poisson's ratio. After Young's modulus and Poisson's ratio are obtained, the material tensor $\mathbf{C}$ [Eq. (8)] can be obtained. Substituting Eqs. (4)–(8) into Eqs. (1)–(3), the governing equations [Eqs. (1)–(3)] are solved by using the finite cloud method (FCM)[15] in this paper.

To validate the use of continuum mechanics theory for the nanoscale structures considered here, we have developed a molecular-dynamics code to solve the equations of motion by using a fifth-order Gear's predictor-corrector algorithm.[16] The simulation time is in the range of 0.2 ns with a time step of 0.5 fs. The MD code uses a Gunsteren-Berendsen thermostat[17] to control the temperature, and neighbor lists to improve the performance of the code.[18] The bonded interactions for the silicon material are modeled with the Tersoff potential.[19] The effect of the doping impurities on the elastic properties of silicon is neglected, as typically the effect of heavy doping is to decrease the elastic constants by 1%–3%.[20] Figure 2 shows Young's modulus as a function of sample cross-sectional area at different temperatures. The temperature-dependent Young's modulus Y obtained by using the molecular-dynamics simulations is compared with that obtained by using an empirical formula, the Varshni function, given in Ref. 21 and shown by the dashed and the dotted lines in Fig. 2. Figure 2 shows that when the cross-sectional area decreases to 9 nm^2, the effective Young's modulus begins to deviate from that of the bulk silicon. This is due to the fact that the surface area-to-volume ratio increases as the structures are miniaturized, and the surface effects become more important. Using the parameterized constants, the continuum mechanics theory is validated by comparing with the classical molecular-dynamics results as shown in Fig. 3. In the MD simulations, the silicon (001) surfaces are reconstructed according to a 2×1 dimmer-row configuration.[22] We also investigated the silicon (001) surface without reconstruction, where the bonds are left dangling on the surface. Figure 4 shows the comparison and we conclude that the surface reconstruction leads to stronger

Downloaded 25 May 2005 to 130.126.121.152. Redistribution subject to AIP license or copyright, see http://jap.aip.org/jap/copyright.jsp

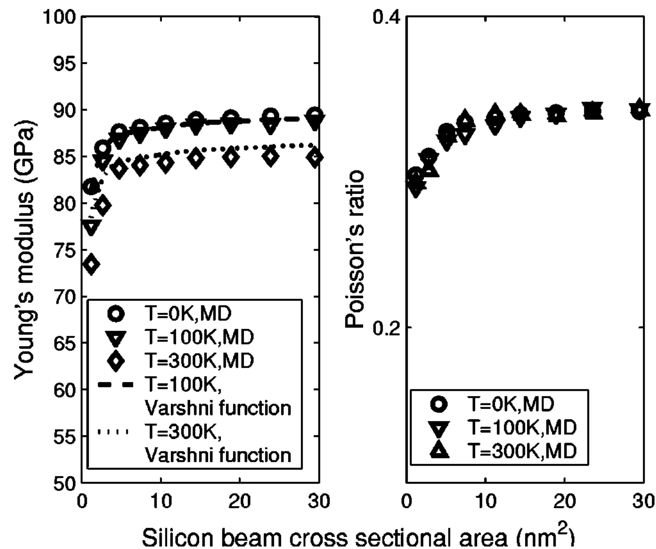

FIG. 2. Young's modulus and Poisson's ratio as a function of the device cross-sectional area. The Varshni function is an empirical formula for Young's modulus which is discussed in Ref. 21.

bonds and hence an increase in the Young's modulus of the material when the cross-sectional area is small. When the cross-sectional area increases, the contribution of the surface bonds will be small and the surface reconstruction effect can be negligible.

IV. ELECTROSTATIC MODELS

The critical dimension in NEMS can vary from several hundred nanometers to just a few nanometers. Appropriate calculation of the electrostatic force on the structures is one of the key issues in the simulation of NEMS. In this section, we show that, depending on the critical dimension of NEMS, three electrostatic models—the classical conductor model, the semiclassical semiconductor model, and the quantum-mechanical model—can be used to compute the electrostatic forces.

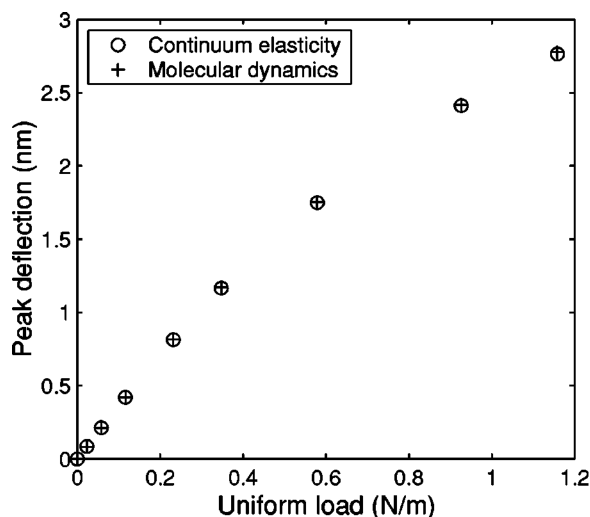

FIG. 3. Peak deflection of a fixed–fixed silicon beam as a function of the applied load. The beam geometry is $32.6\times3.26\times3.26$ nm^3 (length $\times$width$\times$thickness).

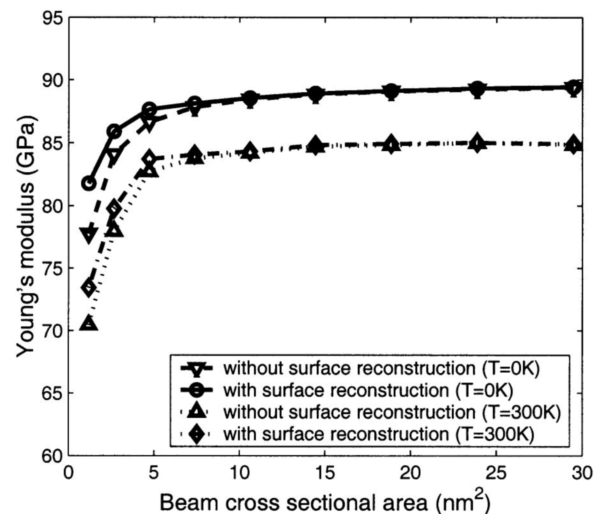

FIG. 4. Young's modulus as a function of the device cross-sectional area. Note that the surface reconstruction leads to an increase in Young's modulus when the cross-sectional area is small.

A. Criteria for different electrostatic models

For real materials, the electrons in solids obey the Fermi–Dirac distribution for different energy states. This means an external electric field can penetrate into the device over a finite distance, namely, the Debye screening length. The Debye screening length, which is also called the characteristic screening length, is defined as[23]

$$\lambda_{ds} = \sqrt{\frac{\epsilon_s k_B T}{e^2 N_D}}, \tag{9}$$

where ϵ_s is the dielectric constant of the semiconductor, e is the elementary charge, k_B is the Boltzmann constant, T is the temperature, and N_D is the doping density. For most of the metals, and for heavily doped semiconductors, the Debye length is estimated to be several angstroms, which is typically much smaller than the geometrical characteristic length of the device. In this case, it is reasonable to assume that the structure is an ideal conductor where all the charges are located on the surface, and the electric potential is constant over the structure. For semiconductor devices with a lower doping density, however, the Debye length can be several tens of nanometers and this can be comparable to the geometrical characteristic length of the device. In this case, the semiconductor structures cannot be treated as ideal conductors and the semiclassical semiconductor model is necessary.

As the geometrical characteristic length of the device continues to shrink, quantum effects become more significant and the carrier concentration at the boundary cannot be described by the semiclassical model due to the effects of carrier quantization.[24] Quantum depletion length, which is the distance from the carrier concentration peak to the surface of the device, is given by[25]

$$\lambda_q \approx \frac{\pi^{3/2}\hbar}{8e}\sqrt{\frac{\epsilon_s}{m^* N_D}}, \tag{10}$$

where $\hbar$ is the reduced Planck's constant, and m^* is the electron effective mass. For nanometer-scale devices, the quan-

Downloaded 25 May 2005 to 130.126.121.152. Redistribution subject to AIP license or copyright, see http://jap.aip.org/jap/copyright.jsp

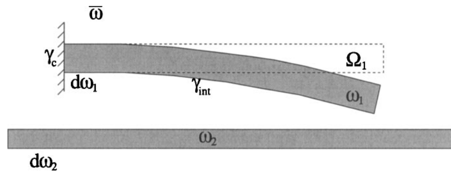

FIG. 5. The electrostatic system.

tum depletion length can be comparable to the geometrical characteristic length. For example, at room temperature (300 K), the quantum depletion length for silicon with $N_D = 10^{18}$ cm^{-3} is about 2.3 nm. When the geometrical characteristic length is comparable to the quantum depletion length, a quantum-mechanical model is needed to accurately compute the charge distribution in the semiconductor structure.

In summary, if the geometrical characteristic length of the system is much larger than the Debye screening length and the quantum depletion length, the classical conductor model is sufficient. When the quantum depletion length is much smaller than the geometrical characteristic length, and the Debye screening length is comparable to the geometrical characteristic length, the semiclassical model can give accurate results. When the quantum depletion length is comparable to the geometrical characteristic length, the quantum-mechanical model will be necessary. These three electrostatic models and their coupling to the elastostatic models are discussed in detail in the following sections.

B. Classical conductor model: Laplace's equation

For metals or heavily doped semiconductor structures, the Debye screening length is quite small. For example, the Debye screening length for silicon with a doping density of 10^{20} cm^{-3} at room temperature (300 K) is estimated to be 0.4 nm. To a high degree of precision, the charge distribution can be modeled as a delta function at the semiconductor-dielectric medium interface and the semiconductor structure can be treated as an ideal conductor. Considering the NEM switch discussed in Sec. II (see Fig. 5 for a simple example), the classical Laplace equation can be used to describe the electric potential field for systems comprised of conductors, i.e.,

$$\nabla \bullet (\epsilon_d \nabla \phi) = 0 \quad \text{in } \bar{\omega}, \tag{11}$$

$$\phi = g_i \quad \text{on } d\omega_{\mathbf{i}}, \quad \mathbf{i} = 1,2 \tag{12}$$

where ϕ is the potential, ϵ_d is the dielectric constant of the dielectric medium, $d\omega_1$ and $d\omega_2$ are the boundaries of the beam structure (ω_1) and the ground electrode (ω_2), respectively, g_1 and g_2 are the potentials prescribed on $d\omega_1$ and $d\omega_2$, respectively, and $\bar{\omega}$ denotes the domain exterior to ω_1 and ω_2. Note that Eq. (11) is defined in the domain exterior to the deformed structures (ω_1 and ω_2). An efficient approach to treat the exterior electrostatic problem is to use a boundary integral formulation (BIE) of the governing equations [Eqs. (11) and (12)],[26] i.e.,

$$\phi(p) = \int_{d\omega} G(p,q)\sigma(q)d\gamma_q + C, \tag{13}$$

$$\int_{d\omega} \sigma(q)d\gamma_q = C_T, \tag{14}$$

where σ is the unknown surface charge density, p is the source point, q is the field point, G is Green's function, $d\omega = d\omega_1 \cup d\omega_2$, C_T is the total charge of the system, and C is an unknown variable which can be used to compute the potential at infinity. In this paper, a boundary cloud method[27] is used to solve the boundary integral equations given in Eqs. (13) and (14) to compute the unknown surface charge density σ. Once the surface charge density is obtained, the electrostatic pressure on the beam surface in the initial configuration can be computed by

$$\mathbf{T} = \frac{\sigma^2}{2\epsilon_d} J\mathbf{F}^{-T}\mathbf{N}, \tag{15}$$

where J is the determinant of the deformation gradient $\mathbf{F}$ (see Ref. 7 for more details). The electrostatic pressure [Eq. (15)] is then applied as the surface traction boundary condition [Eq. (3)] in the mechanical analysis discussed in Sec. III.

C. Semiclassical model: Laplace/Poisson's equations

For semiconductor materials with regular doping, the Debye screening length can be comparable to the critical dimension of the device. In fact, a sufficiently small semiconductor might not be able to screen an external field at all. For example, for silicon with a doping density of $N_D = 10^{18}$ cm^{-3}, $\lambda_{ds} \approx 4$ nm, which may not be negligible for a device with a characteristic length of a few tens of nanometers. In such cases, the induced charges accumulate not only on the surface of the semiconductor but also in the bulk of the semiconductor. As a result, the Poisson equation[24] should be solved in the domain of the beam structure since the source term is not zero due to the volume-distributed charges. The governing equations in the semiclassical model for electrostatic analysis are given by (see Fig. 5 for a better description of where the Poisson and the Laplace equations are solved)

$$\nabla \bullet (\epsilon_s \nabla \phi) = \rho = -e[-n(\phi) + p(\phi) + N_D^+(\phi) - N_A^-(\phi)] \quad \text{in } \omega_1, \tag{16}$$

$$\nabla^2 \phi = 0 \quad \text{in } \bar{\omega}, \tag{17}$$

$$\phi = g_c \quad \text{on } \gamma_c, \tag{18}$$

$$\phi = g_2 \quad \text{on } d\omega_2, \tag{19}$$

$$\epsilon_s \frac{\partial \phi}{\partial \mathbf{n}_{\text{out}}} + \epsilon_d \frac{\partial \phi}{\partial \mathbf{n}_{\text{in}}} = \sigma_{\text{int}} \quad \text{on } \gamma_{\text{int}}, \tag{20}$$

where ρ is the total charge density, N_D^+ and N_A^- are the ionized donor and acceptor concentrations, respectively, and n and p are the electron and hole densities given by

$$n = N_C \frac{2}{\sqrt{\pi}} \mathcal{F}_{1/2}\left(\frac{E_F - E_C}{k_B T}\right), \tag{21}$$

Downloaded 25 May 2005 to 130.126.121.152. Redistribution subject to AIP license or copyright, see http://jap.aip.org/jap/copyright.jsp

$$p = N_V \frac{2}{\sqrt{\pi}} \mathcal{F}_{1/2}\left(\frac{E_V - E_F}{k_B T}\right), \tag{22}$$

where E_F is the Fermi-level energy, $\mathcal{F}_{1/2}$ is the Fermi integral of the order of $1/2$, N_C and N_V are the effective density of states of conduction and valence band, respectively, and E_C and E_V are the conduction- and valence-band energies, respectively. We assume that the ground structure, denoted as ω_2 in Fig. 5, is a conductor and the specified potential on ω_2 is g_2. The specified potential at the fixed end of the beam, denoted as γ_c, is assumed to be g_c. In Eq. (20), $\mathbf{n}_{\text{out}}$ and $\mathbf{n}_{\text{in}}$ are the outward and inward normal vectors at the boundary of the beam, respectively, σ_{int} is the beam/dielectric medium interface charge density, and γ_{int} denotes the interface between the beam and the dielectric medium.

In the exterior domain $\bar{\omega}$, as shown in Eq. (17), Laplace's equation is satisfied. As discussed in Sec. IV B, an efficient approach to treat the exterior electrostatic problem is to use a BIE of Laplace's equation. For semiconductors, the boundary integral equations are given by[28]

$$\alpha(p)\phi(p) = \int_{d\omega} \phi(q) \frac{\partial G(p,q)}{\partial \mathbf{n}_{\text{in}}} d\gamma(q) - \int_{d\omega} \frac{\partial \phi(q)}{\partial \mathbf{n}_{\text{in}}} G(p,q) d\gamma(q) + \phi_{\text{ref}}, \tag{23}$$

$$\int_{d\omega} \frac{\partial \phi(q)}{\partial \mathbf{n}_{\text{in}}} d\gamma(q) = 0, \tag{24}$$

where ϕ_{ref} is the unknown constant reference potential and α is the corner tensor. The potential ϕ and the charge density ρ are obtained by solving Eqs. (16) and (18)–(24) self-consistently. This approach is referred to as the hybrid BIE/Poisson approach (see Ref. 28 for details), where the interior Poisson equation [Eq. (16)] is solved by using FCM[15] and the boundary integral equations [Eqs. (23) and (24)] are solved by the boundary cloud method.[27] Once the potential ϕ and the charge density ρ are computed, the electrostatic body force can be computed by

$$\mathbf{f}_{\text{elec}} = \rho \nabla \phi. \tag{25}$$

By transforming the electrostatic body force on the deformed configuration to the initial configuration, the electrostatic component, $\mathbf{B}_{\text{elec}}$, of the body force vector $\mathbf{B}$ [see Eq. (1)] in the initial configuration is given by[10]

$$\mathbf{B}_{\text{elec}} = J\mathbf{f}_{\text{elec}}. \tag{26}$$

Similar to Eq. (15), the electrostatic pressure $\mathbf{T}$ on the beam surface in the initial configuration is given by

$$\mathbf{T} = \frac{\sigma_{\text{int}}^2}{2\epsilon_d} J\mathbf{F}^{-T}\mathbf{N}. \tag{27}$$

D. Quantum-mechanical model: Laplace/Poisson/Schrödinger's equations

When the size of the device shrinks to nanoscale, quantum effects, such as the carrier quantum confinement in the semiconductor structure, become significant.[24] To account for the quantum effects in the system, Laplace/Poisson's equations given in Sec. IV C are combined with Schrödinger's equation. For the quantum-mechanical model, the hybrid BIE/Poisson approach (see Ref. 28 for details) is extended to include the solution of Schrödinger's equation. By solving the BIE/Poisson/Schrödinger's equations self-consistently, the potential field and the charge distribution in the system can be determined. The two-dimensional effective-mass Schrödinger's equation is given by

$$\hat{H}(\psi_n) = -\left(\frac{\hbar^2}{2m_x^*}\frac{\partial^2}{\partial x^2} + \frac{\hbar^2}{2m_y^*}\frac{\partial^2}{\partial y^2}\right)\psi_n + U(e\phi)\psi_n = E_n\psi_n \quad \text{in } \omega_1, \tag{28}$$

where $\hat{H}$ is the Hamiltonian, $U(e\phi)$ is the potential energy, m_x^* and m_y^* are the effective masses of electrons or holes in the x- and y-direction, respectively, and ψ_n is the wave function corresponding to the energy level E_n. In this paper, we employ $U(e\phi)=E_g/2-e\phi$ for electrons and $U(e\phi)=-E_g/2-e\phi$ for holes, where E_g is the energy gap. By solving Schrödinger's equation [Eq. (28)], the energy levels E_n and the corresponding wave functions ψ_n can be obtained for electrons and holes.

Poisson's equation [Eq. (16)] is coupled with Schrödinger's equation through the quantum electron and hole densities,[29]

$$n_q(\phi) = N_n \sum_n \psi_n^2 \mathcal{F}_{-1/2}\left(\frac{E_F - E_n}{k_B T}\right), \tag{29}$$

$$p_q(\phi) = N_p \sum_n \psi_n^2 \mathcal{F}_{-1/2}\left(\frac{E_n - E_F}{k_B T}\right), \tag{30}$$

where the summation is over all the energy levels and

$$N_n = \frac{1}{\pi}\left(\frac{2m_n^* k_B T}{\hbar^2}\right)^{1/2}, \quad N_p = \frac{1}{\pi}\left(\frac{2m_p^* k_B T}{\hbar^2}\right)^{1/2} \tag{31}$$

for a conduction-band valley and a valence band, respectively. m_n^* and m_p^* are the density-of-state masses of electrons and holes, respectively. Note that, in the quantum-mechanical analysis, the electron and hole densities, n and p, in Eq. (16) are replaced by the quantum electron (n_q) and hole (p_q) densities given in Eqs. (29) and (30). Assuming the semiconductor structure to be an ideal quantum well, we enforce the Dirichlet boundary condition for the wave function, $\psi_n=0$, at the boundary of the semiconductor beam. Schrödinger's equation is solved on the same domain as Poisson's equation, ω_1 (see Fig. 5). Schrödinger's equation is discretized on the deformed configuration by using FCM.[15] The discretized Schrödinger's equation can be rewritten in the matrix form

$$\mathbf{H}\psi_n = E_n\psi_n, \tag{32}$$

where $\mathbf{H}$ is the coefficient matrix obtained by discretizing Eq. (28). The discretized eigenvalue problem, [Eq. (32)], is then solved by using the eigensolver of ARPACK (Ref. 30) to obtain the energy levels and the wave functions of electrons and holes. By using Eqs. (29) and (30), the quantum electron and hole densities can be computed. Table I summarizes the

Downloaded 25 May 2005 to 130.126.121.152. Redistribution subject to AIP license or copyright, see http://jap.aip.org/jap/copyright.jsp

TABLE I. Solution of the coupled Laplace/Poisson/Schrödinger's equations.

(1) Discretize the domain of the semiconductor structure ω_1 and the boundary of the structures $d\omega$.
(2) At the initial step $k=0$, set the initial value of the potential to be $\phi^{(0)}=0$.
(3) Solve Schrödinger's equation [Eq. (28)] by using $\phi^{(0)}$ to compute $\psi_n^{(0)}$ and $E_n^{(0)}$ for electrons and holes.
(4) Compute quantum electron density $n_q^{(0)}$ and hole density $p_q^{(0)}$ [Eqs. (29) and (30)].
(5) **Repeat**
  (a) Solve the coupled BIE/Poisson's equations [Eqs. (16), (18)–(20), (23), and (24)] by using $n_q^{(k)}$ and $p_q^{(k)}$ to obtain potential $\phi^{(k+1)}$.
  (b) Solve Schrödinger's equation [Eq. (28)] by using $\phi^{(k+1)}$ to compute $\psi_n^{(k+1)}$ and $E_n^{(k+1)}$ for electrons and holes.
  (c) Compute the new quantum electron density $n_q^{(k+1)}$ and hole density $p_q^{(k+1)}$ by using Eqs. (29) and (30), respectively.
(6) **until** $|n_q^{(k+1)}-n_q^{(k)}|$ and $|p_q^{(k+1)}-p_q^{(k)}|<$ error tolerance ϵ_t.

procedure for self-consistent electrostatic analysis of NEM structures by using the hybrid BIE/Poisson/Schrödinger approach (see Ref. 28 for more details).

Once we get the potential and the charge density, the electrostatic body force $\mathbf{B}_{\text{elec}}$ and the surface traction $\mathbf{T}$ in the initial configuration can be computed by following the same steps given in Eqs. (25)–(27).

V. VAN DER WAALS INTERACTIONS

van der Waals interactions account for nonbonded interactions between atoms or molecules. The van der Waals energy is computed by using the well-known Lennard-Jones potential[31] which is a spherically symmetric two-body intermolecular potential. The Lennard-Jones potential contains an attractive term and a repulsive term. Since the repulsive term decays rapidly $(1/r^{12})$, it has a significant effect only when the distance between the atoms is close to molecular contact. Hence, we neglect the repulsive term and assume that the pair potential between two atoms is purely attractive and takes the form

$$w(r) = -c/r^6, \tag{33}$$

where r is the distance between the atoms, and c is the van der Waals coefficient. For silicon–silicon interaction, this coefficient is 1.309×10^{-77} Jm^6.[32]

The total van der Waals energy can be calculated by the summation of all the pair atoms in the beam and the ground plane. The cost is about $O(n^2)$, where n is the number of atoms in the system. For NEMS, n is typically over 10^6 and the use of the direct summation method to compute the van der Waals energy during each time step is impractical. We suggest an alternative approach to compute the van der Waals energy by replacing the direct summation with integral quantities. Consider the substrate as layers of two-dimensional continuous plates with each layer having the same number density ρ_p of atoms. The van der Waals energy can then be computed by performing an integration between an atom in the beam and the infinite layers on the substrate region. In practice, just several top layers in the substrate need to be summed separately and all the other layers can be replaced by an integration over the bulk as shown in Fig. 6. The van der Waals energy for the interaction between an atom in the beam and the ground plane is given by

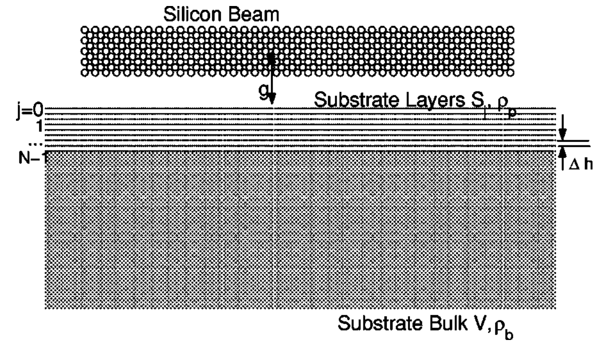

FIG. 6. Layer integration method for the calculation of van der Waals interactions. The ground plane is approximated by layers S_j (perpendicular to the plane of the paper) with surface number density ρ_p and the bulk with the number density ρ_b. g is the gap between the atom in the beam and the top layer of the substrate.

$$\begin{aligned} E_{\text{vdW}} &= \sum_{j=0}^{N-1}\int_{S_j}\frac{c\rho_p}{r^6}dS_j + \int_V \frac{c\rho_b}{r^6}dV \\ &= -\frac{1}{2}\sum_{j=0}^{N-1}\frac{\pi c\rho_p}{(g+j\Delta h)^4} - \frac{1}{6}\frac{\pi c\rho_b}{(g+N\Delta h)^3}, \end{aligned} \tag{34}$$

where N is the number of summation layers in the substrate, S_j is the cross-sectional area of the jth layer, V is the volume of the substrate bulk, g is the gap between the beam and the top layer of the substrate, ρ_p is the surface number density of molecules for the substrate layers, ρ_b is the bulk number density of molecules for the substrate bulk, and $\Delta h = 0.136$ nm is the interlayer distance between two contiguous layers.

The van der Waals force for each atom in the beam is then computed by

$$\begin{aligned} \mathbf{f}_{\text{vdW}} &= \frac{dE_{\text{vdW}}}{dg}(-\mathbf{j}) \\ &= \left[\sum_{j=0}^{N-1}\frac{2\pi c\rho_p}{(g+j\Delta h)^5} + \frac{1}{2}\frac{\pi c\rho_b}{(g+N\Delta h)^4}\right](-\mathbf{j}), \end{aligned} \tag{35}$$

where $\mathbf{j}$ is the unit vector along the y-direction.

The result in Eq. (35) for the computation of van der Waals force on an atom in the beam is compared with the pairwise summation approach in Fig. 7. The forces from both approaches agree very well and the deviation is below 0.8% for a distance of 0.5 nm between the atom and the ground plane. For even smaller gaps between the beam and the ground plane, the deviation would increase significantly as the repulsive term has been neglected.

In the continuum theory, the van der Waals force is applied as a body force. Assuming the beam has the bulk number density ρ_b, the body force component $\mathbf{B}_{\text{vdW}}$ due to the van der Waals interactions in the initial configuration is given by

Downloaded 25 May 2005 to 130.126.121.152. Redistribution subject to AIP license or copyright, see http://jap.aip.org/jap/copyright.jsp

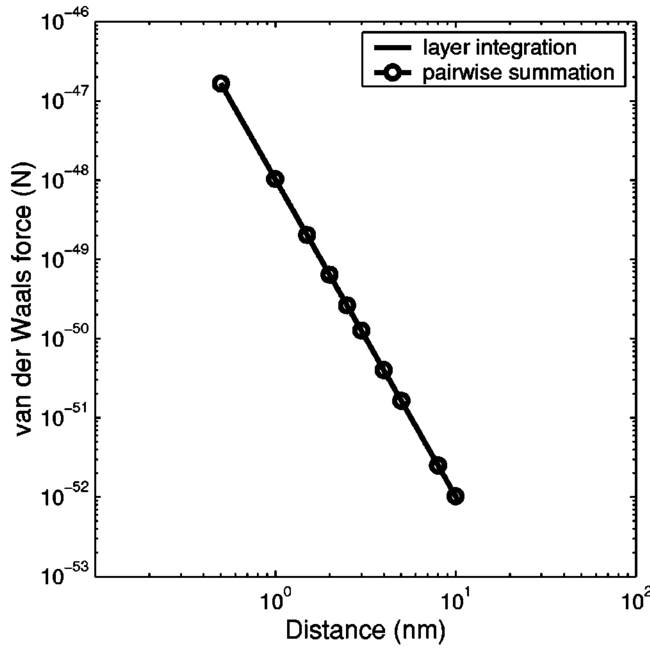

FIG. 7. Comparison of the van der Waals forces given by the continuum approach [Eq. (35)] with that given by the discrete pairwise summation.

$$\mathbf{B}_{\mathrm{vdW}} = J\rho_b \mathbf{f}_{\mathrm{vdW}} = \rho_{b0}\mathbf{f}_{\mathrm{vdW}}, \tag{36}$$

where ρ_{b0} is the bulk number density of the device in the initial configuration.

VI. STRAIN EFFECTS ON ENERGY GAP AND EFFECTIVE MASS

In the presence of strain, the valence bands for silicon may shift or split. This can result in the change of energy gap and effective mass.[33–35] To account for this change, we assume that the strain effect on a finite volume is the same as that on a bulk silicon crystal, as the theory we use here is based on the analysis of a bulk crystal.

We begin by setting up Hamiltonians under the influence of external stresses. The total Hamiltonian H_0 of the valence band with induced strain is given by[34,35]

$$H_0 = H_e + H_k, \tag{37}$$

where H_e is the strain Hamiltonian representing the shift and splitting of the energy bands due to the induced strain and H_k is the effective-mass Hamiltonian which determines the shape of the energy bands at $\mathbf{k}=0$, where $\mathbf{k}$ is the wave vector. The spin-orbit interaction splits the sixfold degenerate into fourfold degenerate states, denoted by $p_{3/2}$, which form the valence-band edge, and twofold degenerate $p_{1/2}$ states. H_e and H_k are 6×6 matrices given by[35]

$$H_e = \begin{bmatrix} H_{11}^e & H_{12}^e \\ H_{21}^e & H_{22}^e \end{bmatrix}, \quad H_k = \begin{bmatrix} H_{11}^k & H_{12}^k \\ H_{21}^k & H_{22}^k \end{bmatrix}, \tag{38}$$

where H_{11}^e is a 4×4 matrix to describe the change within the $p_{3/2}$ multiplets written in terms of the orbital angular momentum $\mathbf{I}$ (Ref. 35),

$$H_{11}^e(\mathbf{e}) = D_0\sum_{i=1}^{3} e_{ii}\hat{I} + \frac{1}{3}D_1\sum_{i=1}^{3} e_{ii}\left(I_i^2 - \frac{1}{3}I^2\right) + \frac{1}{3}D_2\sum_{\substack{i,j=1\\ i\neq j}}^{3} e_{ij}I_iI_j, \tag{39}$$

where $e_{ij}(i,j=1,2,3)$ are the conventional strain components of the strain vector $\mathbf{e}$ (see Ref. 35 for details), $\hat{I}$ is the 4×4 identity matrix, I is the orbital angular momentum operator, I_1, I_2, and I_3 are the three components of I in the x-, y-, and z-directions, respectively, D_0, D_1, and D_2 are the valence-band deformation potentials and their values are given in Ref. 34. Note that I, I_1, I_2, and I_3 are all 4×4 matrices for silicon. The 2×2 block matrix H_{22}^e represents the $p_{3/2}-p_{1/2}$ splitting,

$$H_{22}^e = \begin{bmatrix} -\Lambda & 0 \\ 0 & -\Lambda \end{bmatrix}, \tag{40}$$

where the value of Λ for silicon is 0.044 eV.[36] The 4×2 off-diagonal element H_{12}^e and its transpose conjugate matrix H_{21}^e represent the spin-orbit interactions which can be calculated by decomposing them into basis operators (see Ref. 35, Table I for details). H_{11}^k is a 4×4 matrix given by[35]

$$H_{11}^k = A_0\sum_{i=1}^{3} k_i^2\hat{I} + \frac{A_1}{3}\sum_{i=1}^{3} k_i^2\left(I_i^2 - \frac{1}{3}I^2\right) + \frac{A_2}{3}\sum_{\substack{i,j=1\\ i\neq j}}^{3} k_ik_jI_iI_j, \tag{41}$$

where A_0, A_1, and A_2 are the inverse mass band parameters and their values can be found in Ref. 34, and $k_i(i=1,2,3)$ are the three components of the wave vector $\mathbf{k}$ in the x-, y-, and z-directions. H_{22}^k is a 2×2 matrix given by

$$H_{22}^k = \begin{bmatrix} A_0\sum_{i=1}^{3} k_i^2 & 0 \\ 0 & A_0\sum_{i=1}^{3} k_i^2 \end{bmatrix}. \tag{42}$$

The 4×2 off-diagonal elements H_{12}^k and H_{21}^k can be calculated in the same way as H_{12}^e and H_{21}^e. For a given strain vector, the Hamiltonians H_e, H_k, and H_0 can be obtained by using Eqs. (37)–(42). As discussed in Secs. VI A and VI B, the energy gap and the effective-mass corrections can be determined by computing the eigenvalues and eigenvectors of H_e and H_0.[35] The corrected energy gap and effective mass are then employed in the effective-mass Schrödinger equation given in Eq. (28).

A. Correction of energy gap

The eigenvalues of H_e in Eq. (38) are the valence-band energy states at $\mathbf{k}=0$. Six eigenvalues can be obtained from H_e; however, there are only three different values, i.e., the energy bands of the heavy, light, and split-off holes at $\mathbf{k}=0$ under the influence of external stresses. The highest energy will be the valence-band edge at $\mathbf{k}=0$. Therefore, the correc-

Downloaded 25 May 2005 to 130.126.121.152. Redistribution subject to AIP license or copyright, see http://jap.aip.org/jap/copyright.jsp

TABLE II. Steps for computing the energy-gap correction.

(1) For a given strain, $\mathbf{e}$, compute H_e by using Eqs. (38)–(40).
(2) Compute the eigenvalues of H_e.
(3) The energy-gap correction is given by ΔE_g=maximum eigenvalue of $H_e(\mathbf{e})$.

tion in energy gap due to the strain can be determined by calculating the change of the valence-band edge at $\mathbf{k}=0$.

As an example, considering the case of a hydrostatic pressure P the strain components are given by

$$e_{11}=e_{22}=e_{33}=-(s_{11}+2s_{12})P, \quad e_{12}=e_{13}=e_{23}=0, \tag{43}$$

where s_{11} and s_{12} are cubic compliance constants. The Hamiltonian, H_e in Eq. (38), thus becomes

$$H_e(\mathbf{e})=\begin{bmatrix} -3D_0(s_{11}+2s_{12})P\hat{I} & 0 \\ 0 & H_{22}^e \end{bmatrix}, \tag{44}$$

where $D_0=1.96$ eV for Si[001]. The eigenvalues of H_e in Eq. (44) are $-3D_0(s_{11}+2s_{12})P$ and $-\Lambda$. Note that $-\Lambda$ is the energy for the split-off hole which remains unchanged. The correction in the energy gap due to a hydrostatic pressure is given by

$$\Delta E_g=-3D_0(s_{11}+2s_{12})P \approx -2.43\times 10^{-30}P. \tag{45}$$

This result matches well with the empirical band-gap correction formula given in Ref. 37, i.e.,

$$\Delta E_g=-2.4\times 10^{-30}P. \tag{46}$$

The steps for computing the energy-gap correction are summarized in Table II.

B. Correction of effective mass

Next, we consider the correction for the effective mass due to an arbitrary strain. In Ref. 35, an analytical expression for the energy bands, which is a function of three components of the wave vector $\mathbf{k}$, is derived for cases in which the strains are applied along some simple crystal orientations. In this paper, for an arbitrary induced strain, we numerically calculate the eigenvalues of H_e. From the first-order perturbation theory, the three different eigenenergies of H_0 can be written as[35]

$$E_{\text{heavy}}(\mathbf{k},\mathbf{e})=E^0_{\text{heavy}}(\mathbf{e})+\sum_{i,j} c_{ij}(\mathbf{e})k_ik_j, \tag{47}$$

$$E_{\text{light}}(\mathbf{k},\mathbf{e})=E^0_{\text{light}}(\mathbf{e})+\sum_{i,j} \hat{c}_{ij}(\mathbf{e})k_ik_j, \tag{48}$$

$$E_{\text{split-off}}(\mathbf{k},\mathbf{e})=E^0_{\text{split-off}}(\mathbf{e})+\sum_{i,j} \bar{c}_{ij}(\mathbf{e})k_ik_j, \tag{49}$$

where $c_{ij}(\mathbf{e})$, $\hat{c}_{ij}(\mathbf{e})$, and $\bar{c}_{ij}(\mathbf{e})$, $i,j=1,2,3$, are the unknown coefficients for heavy, light, and split-off holes, respectively. For a given strain vector $\mathbf{e}$, $E^0_{\text{heavy}}(\mathbf{e})$, $E^0_{\text{light}}(\mathbf{e})$, and $E^0_{\text{split-off}}(\mathbf{e})$ are the eigenvalues of H_e as discussed above in Sec. VI A. Next we compute $c_{ij}(\mathbf{e})$, $\hat{c}_{ij}(\mathbf{e})$, and $\bar{c}_{ij}(\mathbf{e})$, $i,j=1,2,3$, by appropriately setting values to k_i, $i=1,2,3$. For example, if we set $k_1=1$, $k_2=0$, and $k_3=0$, c_{11}, $\hat{c}_{11}$, and $\bar{c}_{11}$ can be computed by substituting the values for k_1, k_2, and k_3 into $E_{\text{heavy}}(\mathbf{k},\mathbf{e})$, $E_{\text{light}}(\mathbf{k},\mathbf{e})$, and $E_{\text{split-off}}(\mathbf{k},\mathbf{e})$ in Eqs. (47)–(49), i.e., $c_{11}=E_{\text{heavy}}(\mathbf{k},\mathbf{e})|_{\mathbf{k}=\{100\}^T}-E^0_{\text{heavy}}(\mathbf{e})$, $\hat{c}_{11}=E_{\text{light}}(\mathbf{k},\mathbf{e})|_{\mathbf{k}=\{100\}^T}-E^0_{\text{light}}(\mathbf{e})$ and $\bar{c}_{11}=E_{\text{split-off}}(\mathbf{k},\mathbf{e})|_{\mathbf{k}=\{100\}^T}-E^0_{\text{split-off}}(\mathbf{e})$. Repeating this process, the unknown coefficients c_{ij}, $\hat{c}_{ij}$, and $\bar{c}_{ij}$ can all be determined. For heavy holes, Eq. (47) can be rewritten as[35]

$$\begin{aligned} E_{\text{heavy}}(\mathbf{k},\mathbf{e})-E^0_{\text{heavy}}(\mathbf{e}) &= \{k_1\ k_2\ k_3\}\begin{bmatrix} c_{11} & c_{12} & c_{13} \\ c_{21} & c_{22} & c_{23} \\ c_{31} & c_{32} & c_{33}\end{bmatrix}\begin{Bmatrix} k_1 \\ k_2 \\ k_3 \end{Bmatrix} \\ &= \mathbf{k}^T\mathbf{c}\mathbf{k}=\mathbf{k}^T\mathbf{P}^T\begin{bmatrix} c'_{11} & 0 & 0 \\ 0 & c'_{22} & 0 \\ 0 & 0 & c'_{33}\end{bmatrix}\mathbf{P}\mathbf{k} \\ &= c'_{11}k_1'^2+c'_{22}k_2'^2+c'_{33}k_3'^2, \end{aligned} \tag{50}$$

where k'_1, k'_2, and k'_3 are the components of the transformed wave vector $\mathbf{k}'=\mathbf{P}\mathbf{k}$ along the principle axes x', y', and z', the columns of $\mathbf{P}$ are the eigenvectors of $\mathbf{c}$, and c'_{11}, c'_{22}, and c'_{33} are the eigenvalues of $\mathbf{c}$. The energy band is also given by

$$E_{\text{heavy}}(\mathbf{k},\mathbf{e})-E^0_{\text{heavy}}(\mathbf{e})=\frac{\hbar^2}{2m_x^{*\prime}}k_1'^2+\frac{\hbar^2}{2m_y^{*\prime}}k_2'^2+\frac{\hbar^2}{2m_z^{*\prime}}k_3'^2, \tag{51}$$

where $m_x^{*\prime}$, $m_y^{*\prime}$, and $m_z^{*\prime}$ are the effective masses along the three principal axes x', y', and z', respectively. Therefore, from Eqs. (50) and (51), we obtain

$$m_x^{*\prime}=\frac{\hbar^2}{2c'_{11}(\mathbf{e})}, \quad m_y^{*\prime}=\frac{\hbar^2}{2c'_{22}(\mathbf{e})}, \quad m_z^{*\prime}=\frac{\hbar^2}{2c'_{33}(\mathbf{e})}. \tag{52}$$

The effective masses m_i^* for heavy holes along a given Cartesian coordinate axis $i\in\{x,y,z\}$ are given by[36]

$$\frac{1}{m_i^*}=\frac{(\sin\theta_i\cos\gamma_i)^2}{m_x^{*\prime}}+\frac{(\sin\theta_i\sin\gamma_i)^2}{m_y^{*\prime}}+\frac{(\cos\theta_i)^2}{m_z^{*\prime}}, \quad i=x,y,z, \tag{53}$$

where θ_i is the polar angle of the ith direction from the z'-axis with $0\leqslant\theta_i\leqslant\pi$, and γ_i is the azimuthal angle of the ith direction in the $x'y'$-plane from the x'-axis with $0\leqslant\gamma_i<2\pi$. The algorithm to compute the effective-mass correction for heavy holes is shown in Table III. The effective masses for light and split-off holes can be obtained similarly.

VII. INTEGRATION OF ELASTOSTATIC, ELECTROSTATIC, AND VAN DER WAALS MODELS

In secs. III–VI, we have described mechanical, electrostatic, and van der Waals models for analysis of nanoelectromechanical systems at various length scales. To illustrate the integration of all the models, we show in Table IV a complete algorithm describing the proposed approach for nanoelectromechanical analysis, taking into account the strain effects.

Downloaded 25 May 2005 to 130.126.121.152. Redistribution subject to AIP license or copyright, see http://jap.aip.org/jap/copyright.jsp

TABLE III. Procedure for computing the effective-mass correction for heavy holes.

(1) For a given strain, **e**, compute H_e and H_k by using Eqs. (38)–(42).
(2) Compute the eigenenergy, $E_{\text{heavy}}(\mathbf{k},\mathbf{e})$, of H_0, by using the first-order perturbation theory [Ref. 35].
(3) Compute c_{ii}, $i=1,2,3$, in Eq. (47) by setting $k_i=1$ and $k_j=k_m=0$, $j,m=1,2,3$, and $j,m\neq i$, in $E_{\text{heavy}}(\mathbf{k},\mathbf{e})$.
(4) Compute c_{ij}, $i,j=1,2,3$ and $i\neq j$, in Eq. (47) by setting $k_i=k_j=1$ and $k_m=0$, $m\neq i,j$, in $E_{\text{heavy}}(\mathbf{k},\mathbf{e})$.
(5) Compute the eigenvalues of **c** in Eq. (50) to obtain c'_{ii}, $i=1,2,3$.
(6) Compute the effective masses, $m_x^{*\prime}$, $m_y^{*\prime}$, and $m_z^{*\prime}$, along the principal axes by using Eq. (52).
(7) Compute the effective masses, m_x^*, m_y^*, and m_z^*, along the Cartesian axes, x, y, and z, by using Eq.(53).

VIII. NUMERICAL RESULTS

In this section, we present several results on the static pull-in analysis of NEM switches by self-consistently solving the elastostatic, electrostatic, and van der Waals theories described in the previous sections. From the MD simulations, Young's modulus and Poisson's ratio are retrieved to be 85 GPa and 0.34, respectively, for the bulk Tersoff silicon material. The material constants such as Young's modulus and Poisson's ratio can be strain dependent. However, the strain is typically small ($<2\%$) in the NEMS applications shown in this paper. In fact, as will be shown in the last example of this section, the strain effect on the device pull-in behavior is small. Hence, we use constant values of Young's modulus and Poisson's ratio for all the simulations shown in this paper. All calculations presented in this section are for room temperature (300 K).

A. Example I: Application of the classical electrostatic model

There are a number of NEMS examples where classical electrostatics can produce accurate results. The first example is a silicon beam with a geometry of $2\times0.4\times0.2\ \mu\text{m}^3$ and an initial gap of 20 nm between the beam and the substrate. We consider both fixed–fixed and cantilever beams. Assuming a dopant density of $10^{20}\ \text{cm}^{-3}$, the Debye screening length is approximately 0.4 nm, which is negligible compared with the beam geometry. Therefore, the ideal conductor electrostatic model is applicable for this example. Shown in Fig. 8 is a plot of the gap-peak deflection as a function of the applied voltage for the fixed–fixed NEM switch. Figure 9 shows a plot of the gap-peak deflection as a function of the applied voltage for the cantilever NEM switch. The pull-in voltage for the cantilever beam is 3.2 V, which is much lower than the pull-in voltage of 20.5 V, computed for the fixed–fixed beam.

TABLE IV. A complete algorithm for self-consistent electromechanical analysis of NEMS.

(1) Discretize the domain and the boundary of the semiconductor structures.
(2) **Repeat**
  (a) Do mechanical analysis (on the undeformed geometry) to compute structure displacements.
  (b) Update the geometry of the semiconductors using the computed displacements.
  (c) Compute the corrections for energy gap and effective mass by using the algorithms summarized in Tables II and III (this step can be neglected for small strains).
  (d) Compute the surface charge density and the bulk charge distribution by electrostatic analysis (on the deformed geometry).
  (e) Compute electrostatic pressure and body force (on the deformed geometry).
  (f) Transform the electrostatic pressure and the body force to the original undeformed configuration.
  (g) Compute the van der Waals forces on the deformed geometry and transform them to the original undeformed configuration.
(3) **until** an equilibrium state is reached.

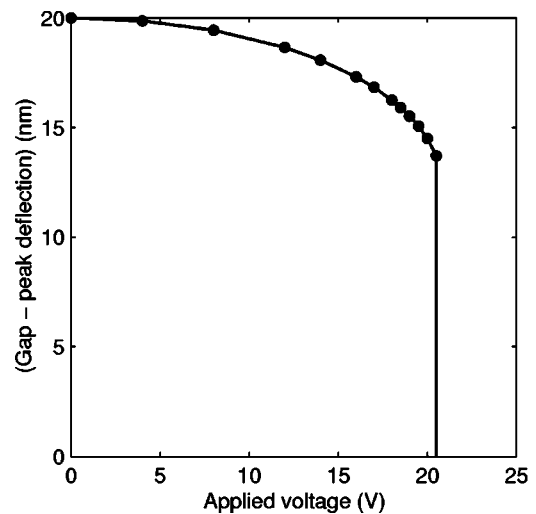

FIG. 8. Gap-peak deflection as a function of the applied voltage for a fixed–fixed beam (geometry of $2\times0.4\times0.2\ \mu\text{m}^3$) with an initial gap of 20 nm.

B. Example II: Application of the semiclassical electrostatic model

When the critical length of the silicon beam decreases to submicron scales or when the doping density of the structure is low, the Debye screening length can become comparable

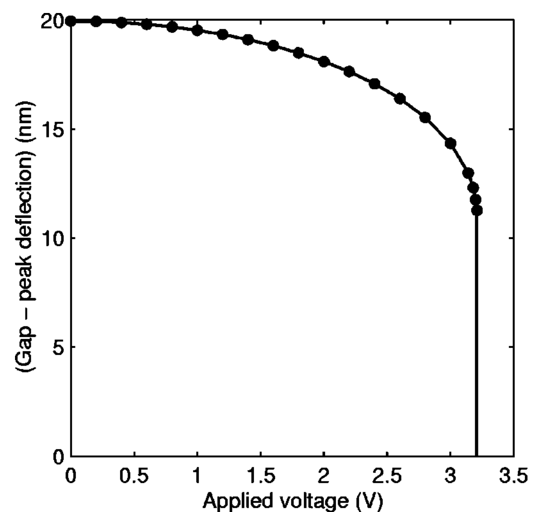

FIG. 9. Gap-peak deflection as a function of the applied voltage for a cantilever beam (geometry of $2\times0.4\times0.2\ \mu\text{m}^3$) with an initial gap of 20 nm.

Downloaded 25 May 2005 to 130.126.121.152. Redistribution subject to AIP license or copyright, see http://jap.aip.org/jap/copyright.jsp

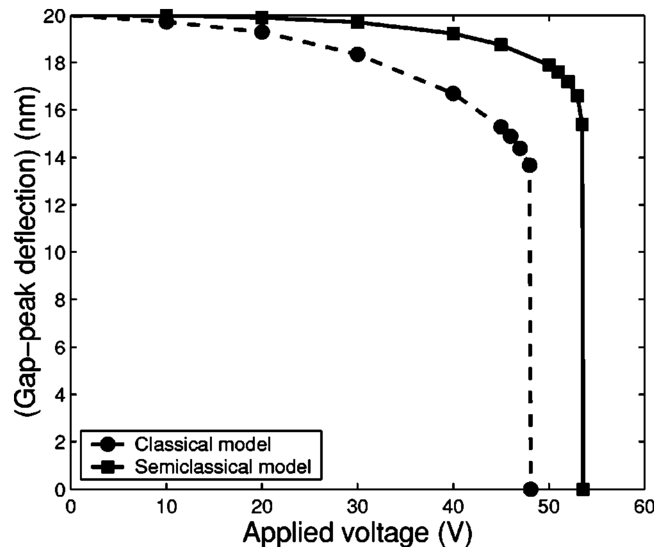

FIG. 10. Gap-peak deflection as a function of the applied voltage for a fixed–fixed beam (geometry of $400\times200\times40$ nm^3) with an initial gap of 20 nm.

to the device critical size. Here we consider a silicon beam with a geometry of $400\times200\times40$ nm^3 and an initial gap of 20 nm between the beam and the substrate. An *N*-type doping density of 10^{18} cm^{-3} is assumed. For this example, the Debye screening length is approximately 4 nm and the semiclassical electrostatic model is necessary. Shown in Fig. 10 is a plot of the gap-peak deflection as a function of the applied voltage for a fixed–fixed NEM switch. Shown in Fig. 11 is a plot of the gap-peak deflection as a function of the applied voltage for a cantilever NEM switch. Figures 10 and 11 also show a comparison between the ideal conductor model and the semiclassical model. From the comparisons in Figs. 10 and 11, we observe that the pull-in voltage computed by the semiconductor model is higher compared to the value obtained with the ideal conductor model. Hence, we can conclude that an ideal conductor model is not accurate when the Debye length is comparable to the critical dimension of the beam.

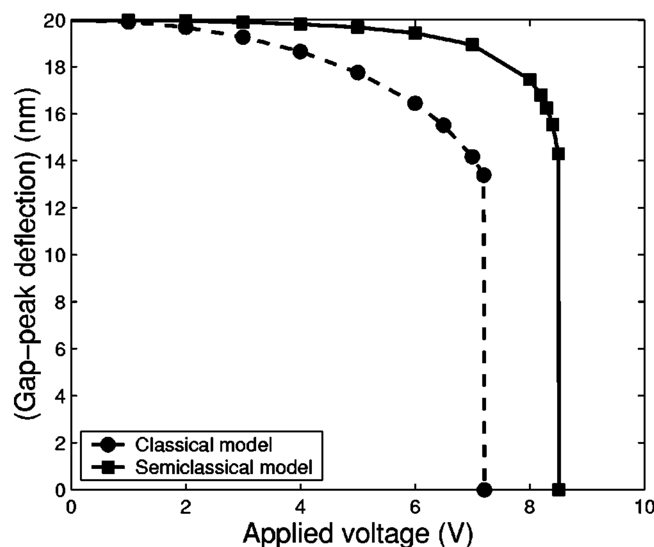

FIG. 11. Gap-peak deflection as a function of the applied voltage for a cantilever beam (geometry of $400\times200\times40$ nm^3) with an initial gap of 20 nm.

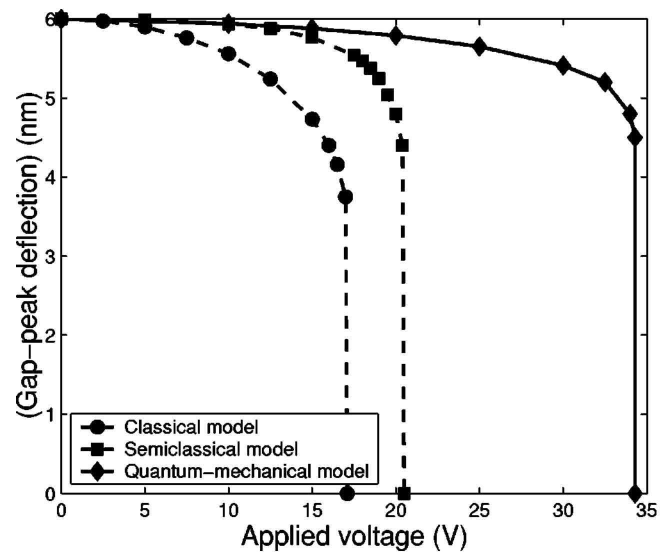

FIG. 12. Gap-peak deflection as a function of the applied voltage for a fixed–fixed beam (geometry of $80\times200\times8$ nm^3) with an initial gap of 6 nm.

C. Example III: Application of the quantum-mechanical model

As the size of the NEM switch further shrinks, the quantum depletion length can become comparable to the system characteristic size, e.g., the gap between the beam and the ground plane. The silicon beam considered here has a geometry of $80\times200\times8$ nm^3 and an initial gap of 6 nm between the beam and the substrate. An *N*-type doping density of 10^{18} cm^{-3} is considered. The quantum depletion length is approximately 2.3 nm which is comparable to the characteristic length of the NEM switch. As a result, a self-consistent solution of the Schrödinger–Poisson equations is necessary for electrostatic analysis. Shown in Fig. 12 is a plot of the gap-peak deflection as a function of the applied voltage for a fixed–fixed NEM switch. Shown in Fig. 13 is a plot of the gap-peak deflection as a function of the applied voltage for a cantilever NEM switch. The comparison with the ideal conductor model and the classical semiconductor model is also shown in these plots. The comparisons indicate that the pull-in voltage computed with the quantum model is significantly higher than the pull-in voltages computed with the ideal conductor and the semiclassical model. Hence, we can conclude that the ideal electrostatic and semiclassical models are not accurate when the quantum depletion length is comparable to the critical length of the NEM switch.

D. Significance of van der Waals forces

van der Waals forces, which can be neglected for MEMS design, can play an important role in NEMS design. To demonstrate this, we consider a silicon beam with a geometry of $80\times200\times8$ nm^3 and an initial gap of 4 nm between the beam and the substrate. The upper subplot shown in Fig. 14 is the gap-peak deflection of the beam as a function of the

Downloaded 25 May 2005 to 130.126.121.152. Redistribution subject to AIP license or copyright, see http://jap.aip.org/jap/copyright.jsp

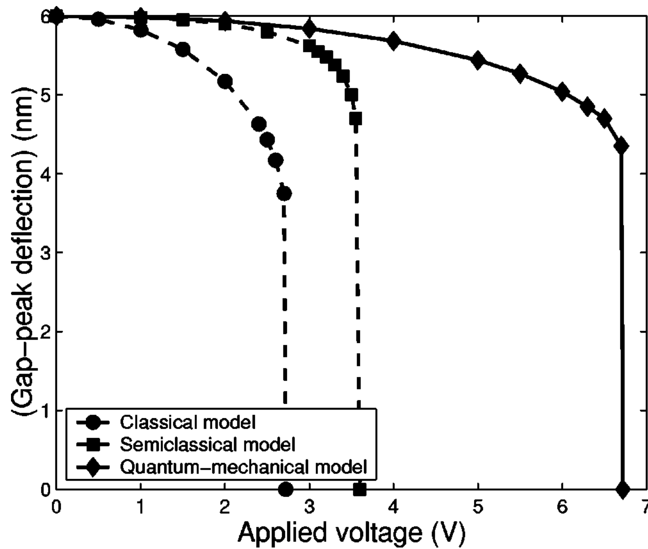

FIG. 13. Gap-peak deflection as a function of the applied voltage for a cantilever beam (geometry of $80\times200\times8$ nm^3) with an initial gap of 6 nm.

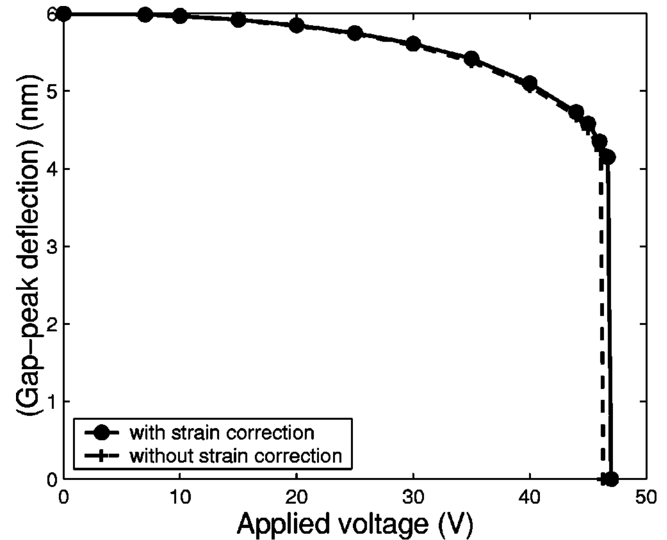

FIG. 15. Gap-peak deflection as a function of the applied voltage for a fixed–fixed switch (geometry of $80\times200\times8$ nm^3) with an initial gap of 6 nm. The solid curve is the result obtained by accounting for the correction of energy gap and effective mass due to the strain. The dashed curve is the result obtained without the corrections.

applied voltage for a cantilever NEM switch. We observe a significant difference in the pull-in voltages obtained with and without the van der Waals forces. Specifically, including the van der Waals forces leads to a smaller pull-in voltage. Even with no applied voltage, we observe that the tip of the beam deflects because of the van der Waals forces. The lower subplot in Fig. 14 shows the variation of the electrostatic and the van der Waals forces as the gap between the beam and the substrate decreases. It is clear that in this example, the van der Waals forces are more dominant compared to the electrostatic forces.

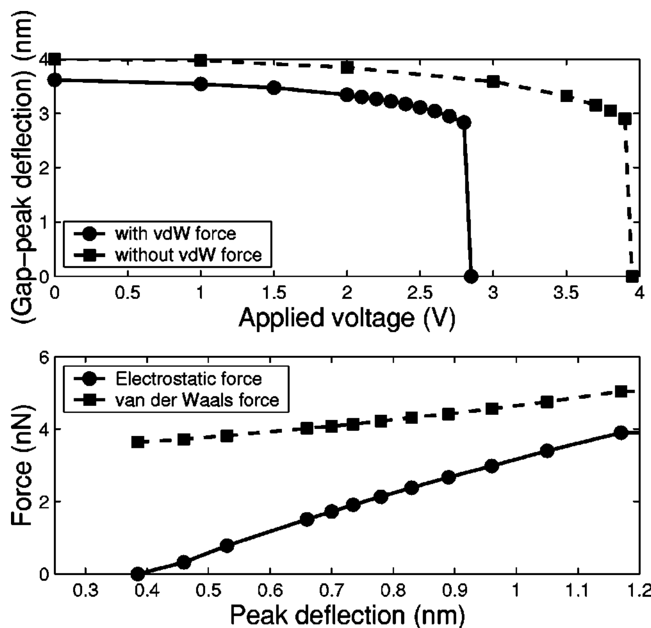

FIG. 14. Effect of the van der Waals force for a cantilever NEM switch with an initial gap of 4 nm. The cantilever beam has the geometry of $80\times200\times8$ nm^3. The lower subplot gives a comparison between the electrostatic force and the van der Waals force as the gap between the beam and the substrate changes.

E. Effect of energy gap and effective-mass correction on pull-in voltages

As discussed in Sec. VI, the energy gap and effective mass can change due to strain. In this section, we solve the quantum-mechanical models by accounting for the strain effects on the energy gap and effective mass. To understand the significance of these corrections, we compare the simulation results with and without such corrections.

We consider a NEM switch which has a beam geometry of $80\times200\times8$ nm^3 and an initial gap of 6 nm between the beam and the substrate. A *P*-type doping density of 10^{18} cm^{-3} is assumed for this example. As the switch dimensions are very small, we use the quantum-mechanical model for electrostatic analysis. Figures 15 and 16 compare the pull-in behavior with and without the corrections for the fixed–fixed and the cantilever beams, respectively. For the cantilever beam since the possible maximum strain (in the order of 10^{-3}) is small, the effect of correction on the device pull-in can be negligible. For the fixed–fixed beam example, a slightly larger pull-in voltage is obtained with the corrections as the fixed–fixed beam can have a larger strain (typically larger than 10^{-2}) compared to the cantilever beam for the same gap.

IX. CONCLUSION

In this paper, we have presented physical models and their numerical implementation for coupled electrical and mechanical analysis of silicon NEMS. The nonlinear continuum elastic theory, with material properties extracted from MD simulations, is combined with either the classical, semiclassical, or the quantum-mechanical electrostatic model and the continuum theory for the van der Waals energy domain to compute the self-consistent electromechanical behavior of silicon NEM switches. We have also presented physical models and their numerical implementation for the change in

Downloaded 25 May 2005 to 130.126.121.152. Redistribution subject to AIP license or copyright, see http://jap.aip.org/jap/copyright.jsp

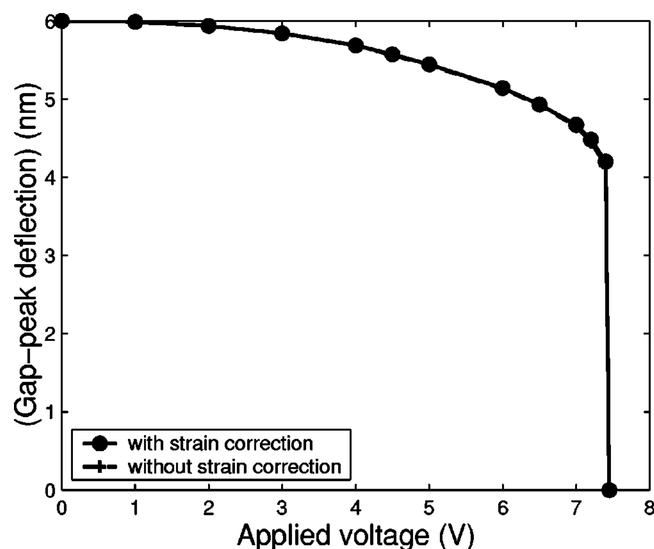

FIG. 16. Gap-peak deflection as a function of the applied voltage for a cantilever beam (geometry of $80\times200\times8$ nm^3) with an initial gap of 6 nm. The solid curve is the result obtained by considering the correction of energy gap and effective mass due to the strain. The dash curve (coincident with the solid curve) is the result obtained without the corrections.

the energy gap and effective mass due to the strain in the silicon nanostructure. Numerical results for silicon NEM switches indicate that the electromechanical characteristics and the pull-in voltage can be sensitive to the electrostatic model employed. In particular, when the characteristic length of the NEM device is comparable to the quantum depletion length, the quantum-mechanical model needs to be employed. When the quantum depletion length is much smaller than the characteristic length but the Debye length is comparable to the characteristic length, then the semiclassical model is appropriate for electrostatic analysis. When the Debye length is much smaller compared to the characteristic length of the NEM device, the classical electrostatic model can be employed. Depending on the nanoswitch geometry (fixed–fixed or cantilever) considered and the gap between the beam and the ground electrode, the van der Waals forces can significantly influence the pull-in voltage and the electromechanical behavior. When the corrections to the energy gap and the effective mass due to the strain in the material are taken into account, a small change in the pull-in voltage is observed for the fixed–fixed beam.

ACKNOWLEDGMENT

We gratefully acknowledge support by the National Science Foundation under Grant No. EEC 0228390.

[1] J. Bryzek, K. Peterson, and W. McCulley, IEEE Spectrum **31**, 20 (1994).
[2] M. L. Roukes, in *Proceedings of the Nanoelectromechanical Systems, Solid-State Sensor and Actuator Workshop*, Hilton Head, 2000, 367–376.
[3] Z. J. Davis, G. Abadal, O. Kuhn, O. Hansen, F. Grey, and A. Boisen, J. Vac. Sci. Technol. B **18**, 612 (2000).
[4] P. Bøggild, T. M. Hansen, C. Tanasa, and F. Grey, Nanotechnology **12**, 331 (2001).
[5] A. N. Cleland and M. L. Roukes, Appl. Phys. Lett. **69**, 28 (1996).
[6] N. R. Aluru and J. White, Sens. Actuators, A **58**, 1 (1997).
[7] G. Li and N. R. Aluru, IEEE Transactions on Computer-Aided Design of Integrated Circuits and Systems **22**, 1228 (2003).
[8] S. K. De and N. R. Aluru, J. Microelectromech. Syst. **13**, 737 (2004).
[9] R. E. Rudd and J. Q. Broughton, Phys. Rev. B **58**, R5893 (1998).
[10] L. E. Malvern, *Introduction to the Mechanics of Continuum Medium* (Prentice-Hall, Englewood Cliffs, NJ, 1969).
[11] R. Phillips, *Crystals, Defects and Microstructures: Modeling Across Scales* (Cambridge University Press, Cambridge, 2001).
[12] J. R. Ray and A. Rahman, J. Chem. Phys. **80**, 4423 (1984).
[13] M. Karimi, H. Yates, J. R. Ray, T. Kaplan, and M. Mostoller, Phys. Rev. B **58**, 6019 (1998).
[14] Z. C. Zhou and B. Joos, Phys. Rev. B **66**, 054101 (2002).
[15] N. R. Aluru and G. Li, Int. J. Numer. Methods Eng. **50**, 2373 (2001).
[16] H. M. Haile, *Molecular Dynamics Simulation* (Wiley, New York, 1992).
[17] H. J. C. Berendsen, J. P. M. Postma, W. F. van Gunsteren, A. DiNola, and J. R. Haak, J. Chem. Phys. **81**, 3684 (1984).
[18] M. P. Allen and D. J. Tildesley, *Computer Simulation of Liquids* (Oxford University Press, New York 1987).
[19] J. Tersoff, Phys. Rev. B **38**, 9902 (1988).
[20] R. Hull, *Properties of Crystalline Silicon* (INSPEC, London, 1999).
[21] Y. P. Varshni, Phys. Rev. B **2**, 3952 (1970).
[22] A. Ramstad, G. Brocks, and P. J. Kelly, Phys. Rev. B **51**, 14504 (1995).
[23] R. F. Pierret, *Semiconductor Device Fundamentals* (Addison-Wesley, Reading, MA, 1996).
[24] K. Hess, *Advanced Theory of Semiconductor Devices* (Prentice-Hall, Englewood Cliffs, NJ, 1988).
[25] A. S. Spinelli, R. Clerc, and G. Ghibaudo, IEEE Trans. Electron Devices **49**, 1314 (2002).
[26] F. Shi, P. Ramesh, and S. Mukherjee, Commun. Numer. Methods Eng. **11**, 691 (1995).
[27] G. Li and N. R. Aluru, Comput. Methods Appl. Mech. Eng. **191**, 2337 (2002).
[28] G. Li and N. R. Aluru, J. Appl. Phys. **96**, 2221 (2004).
[29] A. Trellakis, A. T. Galick, A. Pacelli, and U. Ravaioli, J. Appl. Phys. **81**, 7880 (1997).
[30] http://www.caam.rice.edu/software/ARPACK/
[31] J. E. Lennard-Jones, Proc. R. Soc. London, Ser. A **129**, 598 (1930).
[32] J. Colchero, E. Meyer, and O. Marti, *Handbook of Micro/Nanotribology*, 2nd ed. (CRC, Cleveland, 1999), p. 273.
[33] W. H. Kleiner and L. M. Roth, Phys. Rev. Lett. **2**, 334 (1959).
[34] J. C. Hensel and G. Fener, Phys. Rev. **129**, 1041 (1963).
[35] H. Hasegawa, Phys. Rev. **129**, 1029 (1963).
[36] C. Kittel, *Introduction to Solid State Physics*, 7th ed. (Wiley, New York, 1996).
[37] W. Paul and D. M. Warschauer, *Solids under Pressure* (McGraw-Hill, New York, 1963).

Downloaded 25 May 2005 to 130.126.121.152. Redistribution subject to AIP license or copyright, see http://jap.aip.org/jap/copyright.jsp